Received: 23 November 2019 | Accepted: 13 April 2020

DOI: 10.1002/vzj2.20029

Vadose Zone Journal

ORIGINAL RESEARCH ARTICLES

On the impact of increasing drought on the relationship between soil water content and evapotranspiration of a grassland

Mehdi Rahmati[1,2] | **Jannis Groh**[2,3] | **Alexander Graf**[2] | **Thomas Pütz**[2] | **Jan Vanderborght**[2] | **Harry Vereecken**[2]

[1]Dep. of Soil Science and Engineering, Faculty of Agriculture, Univ. of Maragheh, Maragheh, Iran

[2]Agrosphere Institute IBG-3, Forschungszentrum Jülich, Jülich, 52425, Germany

[3]Research Area 1 "Landscape Functioning," Working Group "Hydropedology," Leibniz Centre for Agricultural Landscape Research (ZALF), Müncheberg, 15374, Germany

Correspondence
Mehdi Rahmati, Dep. of Soil Science and Engineering, Faculty of Agriculture, Univ. of Maragheh, Maragheh, Iran.
Email: mehdirmti@gmail.com
Harry Vereecken, Agrosphere Institute IBG-3, Forschungszentrum Jülich, 52425 Jülich, Germany.
Email: h.vereecken@fz-juelich.de

Abstract

Weighable lysimeters were used to study the relation between soil water content (SWC) and the actual evapotranspiration (ET_a) of grassland under two different climate regimes of Rollesbroich and Selhausen but for an identical soil from Rollesbroich. All components of the water balance were determined from 2012 until 2018. Budyko analysis was used to characterize the hydrological status of the studied sites. Wavelet analysis was also applied to study the power spectrum of ET_a, vegetation-height-adjusted reference evapotranspiration (ET_{crop}), and water stress index (WSI) defined as ET_a/ET_{crop}, as well as SWC at three different depths and the coherence between SWC and ET_a and WSI. The Budyko analysis showed that 2018 resulted in a shift of both locations towards more water-limited conditions, although Rollesbroich remained an energy-limited system. Based on the power spectrum analysis, the annual timescale is the dominant scale for the temporal variability of ET_a, ET_{crop}, and SWC. The results also showed that increasing dryness at the energy-limited site led to more temporal variability of SWC at all depths at the annual timescale. Wavelet coherence analysis showed a reduction of the phase shift between SWC and ET_a at an annual scale caused by the increase in dryness during the measurement period. We found that phase shifts between SWC and ET_a and SWC and WSI were stronger at the water-limited site than at the energy-limited site. The wavelet coherence analysis also showed that from 2014 to 2018, the control of ET_a and WSI on SWC increased due to higher dryness of soil.

1 | INTRODUCTION

The interaction between soil water content (SWC) and actual evapotranspiration (ET_a) plays a key role in ecohydrological and land-surface processes (Robinson et al., 2008; Scanlon et al., 2006; Wang & Dickinson, 2012; Wang, Wang, & Zhang, 2019). Although the relationship between SWC and ET_a is critical for land–atmosphere coupling and management of agroecosystems, the key processes are not yet well understood (Miralles, Gentine, Seneviratne, & Teuling, 2019). Land surface energy dynamics, regional runoff dynamics, and vegetation productivity can be strongly affected by variations in SWC (Moran, Peters-Lidard, Watts, & McElroy, 2004). In

Abbreviations: EI, evaporative index; ET, evapotranspiration; ET_a, actual evapotranspiration; ET_{crop}, vegetation-height-adjusted reference evapotranspiration; ET_0, reference evapotranspiration; SWC, soil water content; SWS, soil water storage; TERENO, German Terrestrial Environmental Observatories; WP, wilting point; WSI, water stress index.

particular, the effect of longer drought periods on the interaction between SWC and ET_a requires further analysis, and its improved understanding is key for sustainable management of agricultural production systems such as grass- and arable lands.

Several studies, based on observations and model predictions, pointed out the major impact of SWC on ET_a (Jung et al., 2010; Seneviratne et al., 2010; Teuling et al., 2009) across spatial scales. At a global scale, Jung et al. (2010) showed that limited soil water supply led to a decline in global land ET_a. They based their analysis on meteorological observations, using remotely sensed SWC and ET measurements obtained from the global FLUXNET in combination with ensemble calculations of different land surface models. The time period that a soil, as a large reservoir, is able to remember past anomalies of SWC is considered as SWC persistence or memory (Orth, 2013). Orth and Seneviratne (2013) used data from >100 catchments across Europe to study the impact of SWC memory (persistence characteristic) on ET_a and runoff. Memory effects are typically studied using autocorrelation of observed or modeled SWC time series (McColl, He, Lu, & Entekhabi, 2019). Orth and Seneviratne (2013) found higher memory effects for monthly averaged data of SWC and ET than for daily averaged values, because the monthly aggregation takes out the daily variations of meteorological effects. They also showed that SWC memory is stronger during drying anomalies and that SWC memory acts as an upper limit for ET memory. Graf et al. (2014) applied wavelet coherence analysis on SWC and all major water budget components including precipitation (P), reference evapotranspiration (ET_0), ET_a, and runoff in an energy-limited site (Wüstebach, Germany) for a period of 3 yr from 1 May 2010 to 30 Apr. 2013. They found out that at weekly resolution, soil water storage (SWS) is correlated to the residual of P–ET–runoff and that the variation in the coherence between SWC and ET_a/ET_0 in time is responding to changes in soil water availability.

Although the abovementioned studies outline the importance of SWC control on ET_a and the control of SWC memory on ET_a, the strength of SWC control on ET_a is uncertain. To address this, Seneviratne et al. (2010) reviewed the role of SWC on land surface–climate interactions in a changing climate with a specific focus on SWC–temperature (T) and SWC–P feedbacks. They identified three climate or SWC regimes that control the SWC–ET_a coupling: a wet SWC regime with SWC values above a critical value, a dry SWC regime with SWC below wilting point (WP), and a transitional climate regime between a critical SWC and WP where SWC strongly controls ET_a. The dry and transitional regimes correspond to the water-limited ET_a regime defined in the Budyko theory (Budyko & Miller, 1974), whereas the wet regime corresponds to the energy limited ET_a regime in this theory. Seneviratne et al. (2010) concluded that there is still a large uncertainty with respect to the impact of geographical position and transitional climate regimes on the control of SWC on ET_a.

Core Ideas

- Both examined sites shifted toward more water-limited conditions in dry year 2018.
- The yearly phase shift between SWC and ET_a decreased by greater dryness of 2014–2018.
- The control of ET_a and WSI on SWC increased by greater dryness of 2014–2018.

Only a few studies examined the phase shift between SWC and ET_a, most of them based on simulation studies. Phase shift is one of the most useful criteria to investigate the interplay between two time series data (signals). It quantifies the time difference of two consecutive maxima of investigated signals (Si, 2008), which allows to identify which variable controls the other. Feng, Porporato, and Rodriguez-Iturbe (2015) used a stochastic model of soil water balance to quantify the phase difference analysis between SWC and ET_a. Their results show that in dry conditions, annual ET_a increases if P and ET_0 are in phase. Li, Liang, Zhang, and Liu (2016) used the SWAT model to quantify spatial–temporal variations in SWC and ET_a in the Yellow River basin, a large water-limited basin in China. They found that SWC lagged behind ET_a by up to 3 mo and that delays were shorter in drier areas.

Wavelet coherence analysis provides a proper tool to investigate the dynamics of the relationships between SWC and ET_a including lagged or in phase relationships (Si, 2008).

In this paper we analyze the relationship between SWC and ET_a over a 7-yr period for a grassland soil under two different climates using data obtained from weighable lysimeter systems, applying wavelet coherence analysis. The investigated time window includes the four warmest years in the global temperature record, 2015–2018 (WMO 2019), as well as the second driest period on record in Germany between April and September 2018 (WMO 2019). The objectives of this study were (a) to analyze the dynamics of the SWC–ET_a and SWC–WSI relationship in time and frequency domains from daily to yearly timescales under different climates for the same soil, and (b) to study the coherence and phase shift between SWC and ET_a, as well as SWC and WSI.

2 | MATERIALS AND METHODS

2.1 | Study sites

The data were collected at the experimental field sites Rollesbroich (50°37′12″ N, 6°18′15″ E) and Selhausen

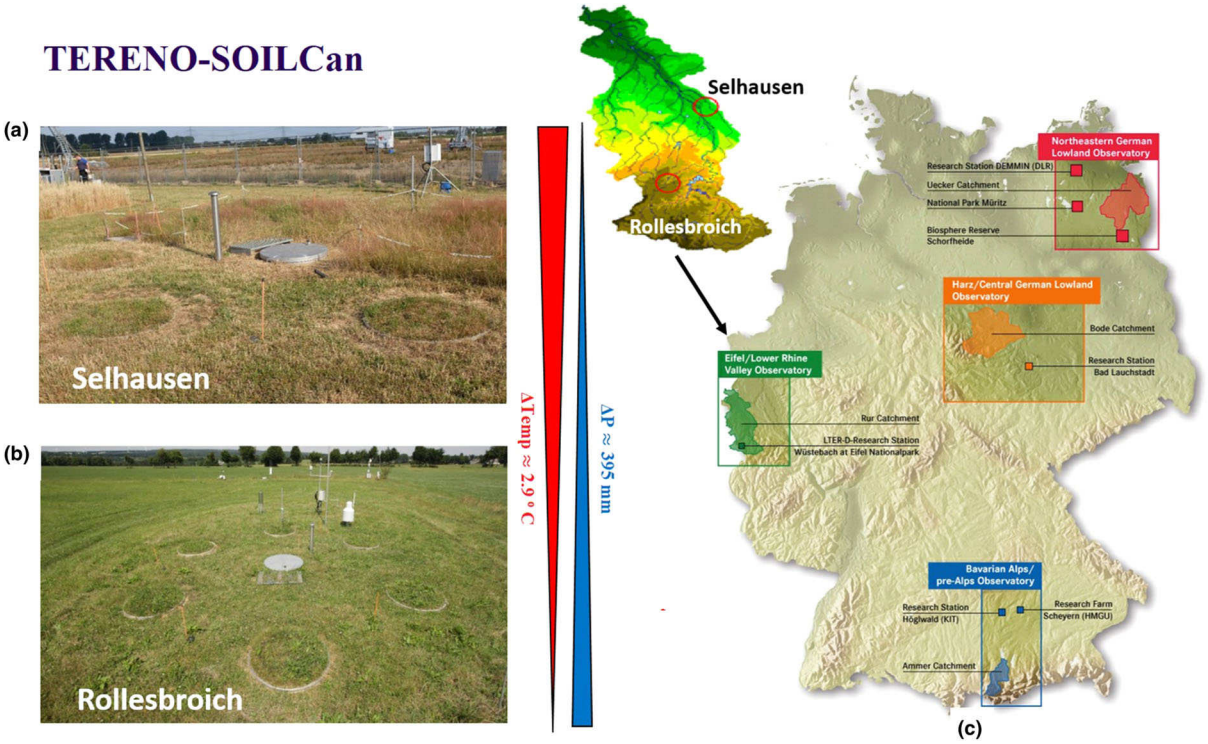

FIGURE 1 Study sites of (a) Selhausen and (b) Rollesbroich located in Eifel/Lower Rhine Valley (c) of the German Terrestrial Environmental Observatories (TERENO) in Germany (modified from Pütz et al., 2016). The ΔTemp and Δ*P* are the changes in temperature and precipitation, respectively. The abbreviation DEMMIN stands for Durable Environmental Multidisciplinary Monitoring Information Network, DLR stands for German Aerospace Center, LTER-D stands for German Long Term Ecological Research, KIT stands for Karlsruhe Institute of Technology, and HMGH stands for German Research Center for Environmental Health

(50°52′7″ N, 6°26′58″ E) located at the Eifel/Lower Rhine Valley Observatory of the German Terrestrial Environmental Observatories (TERENO) in Germany (Figure 1; Bogena et al., 2018; Pütz et al., 2016). Hereafter, for convenience we will call Rollesbroich the energy-limited site and Selhausen the water-limited site (see Section 3). We used nine weighable high-precision grassland lysimeters taken at the energy-limited site, which are part of the TERENO-SOILCan lysimeter network in Germany (Pütz et al., 2016). Six of the lysimeters filled with soil monoliths were installed in spring 2010 at their original location in winter 2010, and three monolithical lysimeters were transferred from energy-limited site to the water-limited site, to subject them to a drier and warmer climate, in winter 2010. Lysimeter data for 2011 were not included in the evaluation because at least one hydrological year is necessary for the lysimeters to adapt to the prevailing site conditions. The transfer from an elevated site (Rollesbroich, 515 m asl) along an altitudinal gradient to a lowland site (Selhausen, 104 m asl) corresponded to an increase of the average daily temperature of 2.9 °C and a decrease of the average annual *P* of 395 mm during the study period (2012–2018). All lysimeters have a surface area of 1 m^2 and a depth of 1.5 m. The extensively managed grassland ecosystem consists mainly *Lolium perenne* L. and *Trifolium repens* L. In order to prevent the disruption of the natural hydraulic gradient and water flow by the lysimeter vessel, tensiometers (TS1, UMS) were installed at 1.4-m depth in the lysimeters and in the surrounding field soil. The field tensiometers controlled a bidirectional pump to transport water upwards (capillary rise) or downwards (drainage) between a suction rake at the lysimeter bottom and the seepage water tank and ensured that the lysimeter water dynamics were adjusted to the observed field dynamics (Groh, Vanderborght, Pütz, & Vereecken, 2016). Further information of the test site and the lysimeter setup is available in Pütz et al. (2016).

2.2 | Time series data

Seven-year time series data (1 Jan. 2012–31 Dec. 2018; i.e., 2,557 d) were obtained from different sources in this study. The ET_a data were calculated from weight changes of lysimeters, which provide 1-min mass changes with resolution of 10 g. The raw data underwent an extensive manual and automated plausibility check. For more details, see Küpper et al. (2017) and Pütz et al. (2016). Consequently, the adaptive window and threshold filter (AWAT; Peters et al., 2017) was used for further noise reduction, which negatively affects the

determination of land surface water fluxes. The AWAT filter applies an adaptive smoothing window and adaptive threshold value to the lysimeter data, which are both dependent on the noise and signal strength of measurements. To further omit an underestimation of fluxes during changes in flow direction, a snap routine was implemented in the AWAT filter routine, which adds an additional anchor point between the original points, based on the 75th quantile of the neighboring moving average data. This routine has been shown to reliably estimate water fluxes, especially for flux events like dew formation or small ET in winter (Groh, Pütz, Gerke, Vanderborght, & Vereecken, 2019; Groh et al., 2018). We used the procedure referred to above to obtain daily ET_a data from energy-limited site and water-limited site for 2013–2018 and 2015–2018, respectively. To obtain ET_a for the remaining years (2012 in the energy-limited site and 2012–2014 in the water-limited site), the ET_a was calculated based on the daily water balance equation (Groh et al., 2020):

$$ET_a = P - \Delta SWS - Q_{net} \quad (1)$$

where P is daily precipitation, Q_{net} is the daily sum of net water flux across the lysimeter bottom ($Q_{net} > 0$: drainage; $Q_{net} < 0$: capillary rise) and ΔSWS is the daily SWS change in the soil profile, which was obtained by analyzing the changes of lysimeter weight at night (mean value of weight between 12:00 a.m. and 2:00 a.m.) between two consecutive days. This approach was necessary, because the sealing covering the gap between the lysimeter cylinder and the collar affected the intra-daily weight measurement of the lysimeters due to changes in properties of the sealing by sunlight. However, measurements at night were accurate.

We obtained the daily Q_{net} values from mass changes of the leachate from the lysimeters, collected with a weighable reservoir tank (resolution = 1 g). The SWC of the lysimeters is measured at three different depths (10, 30, and 50 cm) using time- domain reflectometry probes (CS610, TDR100, Campbell Scientific) with a 30-min time interval.

We obtained the meteorological data from the TERENO data portal (https://teodoor.icg.kfa-juelich.de/ibg3searchportal2/index.jsp). The stations of the used data are listed in Supplemental Material 1. The meteorological data comprised T and wind speed measured at 2-m height, as well as relative and specific humidity, air pressure, and global radiation. All variables were averaged daily prior to any further analysis. Then, crop adjusted reference evapotranspiration (ET_{crop}, Equation 2), as well as the reference grass surface evapotranspiration with a reference height of 12 cm (ET_0, Equation 3), were calculated using the Penman–Monteith model on a daily basis after Allen, Pereira, Raes, and Smith (1998). Equation 3 is derived from the original Penman–Monteith Equation 2 to estimate ET_0 (Allen et al., 1998):

$$ET_{crop} = \frac{\Delta\left(R_n - G\right) + \rho_a c_p (e_s - e_a)/r_a}{\lambda\left[\Delta + \gamma(1 + r_s/r_a)\right]} \quad (2)$$

$$ET_0 = \frac{0.408\Delta\left(R_n - G\right) + \gamma\frac{900}{T+273}u_2(e_s - e_a)}{\Delta + \gamma(1 + 0.34u_2)} \quad (3)$$

where ET_{crop} and ET_0, respectively, are vegetation-height-adjusted and reference grass evapotranspiration (mm d^{-1}), λ is latent heat of vaporization (MJ kg^{-1}), R_n is net radiation at the crop surface (MJ m^{-2} d^{-1}), and G is soil heat flux density (MJ m^{-2} day^{-1}). We ignored G in our calculations ($G = 0$), since its value beneath the grass surface is relatively small in magnitude during a day (Allen et al., 1998). The symbols e_s and e_a, respectively, are saturation and actual vapor pressures (kPa), $e_s - e_a$ is saturation vapor pressure deficit (kPa), Δ is the slope of saturation vapor pressure curve (kPa $°C^{-1}$), γ is psychrometric constant (kPa $°C^{-1}$), ρ_a is mean air density (kg m^{-3}), and c_p is specific heat (MJ kg^{-1} $°C^{-1}$). T is mean daily air temperature at two meters height (°C) and u_2 is wind speed at 2-m height (m s^{-1}). The r_s and r_a respectively are (bulk) surface or canopy and aerodynamic resistances (s m^{-1}).

The plant heights of the grassland varied considerably during the season. In the case of ET_{crop}, the variables of r_a, r_s, and leaf area index (LAI) (Allen et al., 1998) were estimated based on measured height of the grassland vegetation:

$$r_a = \frac{\ln\left[\left(z_m - 2/3h_{plant}\right) / \left(0.123h_{plant}\right)\right] \times \ln\left\{\left(z_m - 2/3h_{plant}\right) / \left[0.1\left(0.123h_{plant}\right)\right]\right\}}{k^2 u_2} \quad (4)$$

$$r_s = r_i/LAI_{act} \quad (5)$$

$$LAI_{act} = 0.5LAI = 0.5\left(24h_{plant}\right) \quad (6)$$

where z_m and z_h are the heights of the wind and humidity measurements (L), respectively, h_{plant} is the grass height (m) at the lysimeter, and k is the von Karman constant (–). The stomatal resistance, r_i (s m^{-1}), was fixed to 100 s m^{-1} assuming a well-watered grass cover according to Allen et al. (1998). The LAI_{act} is the active leaf area index taking into account that only the upper grass surface contributes to heat and vapor transfer (–). We measured the grass heights at the lysimeters by measuring stick and linearly interpolated the heights between two measurements intervals on a daily basis.

2.3 | Data gap filling

Missing meteorological data were gap-filled using an Empirical Orthogonal function (EOF) approach after Beckers and Rixen (2003) and modified by Graf (2017). We used the local TERENO network of 18 meteorological stations to set up a correlation matrix between sites for each variable, and filled the missing data by iterative re-estimation based on the significant EOFs, which were in turn determined by cross-validation.

Missing ET_a and SWC data were gap filled by applying the group method of data handling (GMDH; Hecht-Nielsen, 1990), which has been successfully used to gap fill series of soil hydrological state variables (Pachepsky & Rawls, 1999; Rahmati, 2017). In the case of ET_a, we used available ET_0 data for the same day, as well as available ET_a data for 2 d before and 2 d after missing dates as predictors. For SWC, we used the available SWC data from neighboring stations as predictors from the TERENO platform. The details about the gap filling of the time series data, as well as the quality of the gap-filled data, are provided in Supplemental Material 2.

2.4 | Data analysis

2.4.1 | Data averaging

In our analysis, we used lysimeter-averaged daily data of the soil water balance at the energy-limited site (six lysimeters) and water-limited site (three lysimeters). We used the CV to quantify the variability between lysimeters. The CV values of SWC were calculated for the three depths by averaging the values over the whole measurement period and deriving an averaged SD. At the energy-limited site, the CV values of SWC were 5, 4.5, and 7.0% at the depths 10, 30, and 50 cm, respectively. At water-limited site, the CV values were 8.2, 7.1, and 3.1% at 10, 30, and 50 cm. In the case of ET_a, the CV values at energy-limited and water-limited sites were 10.5 and 8.2%, respectively. The SWC and ET_a are therefore slightly more variable at the water-limited site than at the energy-limited site. Overall, given the low CV values, the mean values are a good representation of SWC and ET_a of single lysimeters.

2.4.2 | Consistency check of actual evapotranspiration data

Prior to averaging across lysimeters, we applied a consistency check on daily ET_a data obtained from the different lysimeters at each site. To do this, we conducted an ANOVA on ET_a data based on a completely randomized design with the factors lysimeter and time. Then, we analyzed the residuals (e) obtained from ANOVA analysis. The hypothesis was that the residuals are normally distributed. To check this, we first calculated the cumulative probability (p) of the e values. Then, taking the mean and SD of the e, we recomputed the normally distributed residuals ($\hat{e}$) for the obtained p values. Then, we considered the data with $e < \min(\hat{e})$ or $e > \max(\hat{e})$ as outliers and removed them. This led to the removal of 32 daily lysimeter ET_a values in the energy-limited site and 75 in the water-limited site. Finally, we used the mean value of the remaining lysimeters for each day to gap fill those data, or a simple regression between ET_a and ET_{crop} was used to replace them in the case that all lysimeters of a given day were taken out.

2.4.3 | Budyko plot

We used the Budyko framework (Budyko, 1958; Budyko & Miller, 1974) to characterize the hydrological status of both sites. In a Budyko plot, the evaporative index ($EI = ET_a/P$) is plotted against the aridity index ($AI = ET_{crop}/P$) for annual or long-term averages.

2.4.4 | Soil water storage and water stress index

In order to quantify the SWS, we used SWC measured at three different depths of 10, 30, and 50 cm. To do this, we used the following equation:

$$SWS = SWC\{10\ cm\} \times d_1 + SWC\{30\ cm\} \times d_2 + SWC\{50\ cm\} \times d_3 \quad (7)$$

where SWS is soil water storage (L) of the entire soil profile (150-cm depth), SWC is soil water content ($L^3\ L^{-3}$) at different depths specified by {10 cm}, {30 cm}, and {50 cm}, and d_1–d_3 represent the layer thickness. We assume that SWC{10 cm} is reflecting the soil water status in Layer 1 from soil surface to 20-cm depth ($d_1 = 20$ cm), SWC{30 cm} is reflecting the soil water status in Layer 2 from 20- to 40-cm

depth, and finally SWC{50 cm} is reflecting the soil water status in the last layer from 40- to 150-cm depth.

To characterize the occurrence of water stress, we used the ratio between ET_a and ET_{crop} as the water stress index (WSI) (Eden, 2012; Speich, 2019). Water stress index values <1 reflect conditions when the plant can no longer transpire optimally and reduces its transpiration rate. Our calculations showed large variability in WSI values, especially in wintertime, including values >1. This is likely the result of comparatively large error to signal ratios on both the enumerator and denominator, as both ET_a and ET_{crop} are small in wintertime. For example, winter *P* is occurring at times when plants are senesced or are not transpiring. During the summer time (1 July–30 September), 95% of WSI values were between 0.05 and 1.2 in both sites. Therefore, as it is unrealistic to have WSI values >1, we limited all WSI values >1 to 1.

2.4.5 | Wavelet analysis

Continuous wavelet coherence analysis (Si, 2008) was used to quantify the strength of correlation and phase shift (delay) between SWC and ET_a and between SWC and WSI for each point in the time and in the frequency domain. The software package described in Grinsted, Moore, and Jevrejeva (2004) was used to conduct the wavelet coherence analysis, where a Monte Carlo approach is used to determine the significance of localized coherence (Graf et al., 2014). The continuous, nonorthogonal Morlet wavelet is selected as the mother wavelet function (Graf et al., 2014; Grinsted et al., 2004).

According to Si (2008), the integral wavelet transform, $W(s, \tau)$ of a time series $y(t)$ measured at time t is defined by

$$W(s,\tau) = \int y(t)\frac{1}{\sqrt{s}}\Psi^*\left(\frac{t-\tau}{s}\right)\mathrm{d}t \tag{8}$$

where ψ^* is the mother wavelet function, s is the dilation ($s > 1$) or contraction ($s < 1$) factor of the wavelet function ψ^*, and τ is the temporal translation or shift of the function ψ^* (Si, 2008). The squared amplitude of the wavelet transform, $|W(s, \tau)|^2$, gives the wavelet power spectrum (Torrence & Compo, 1998). One can plot this spectrum against time, providing delocalized information of the power at a certain moment in time, or against frequency or period. We must note that in addition to the original signals, we also conducted a power spectrum analysis on normalized signals (dividing signals by their SD). In this case, the SWC spectra almost coalesce. The larger variance at 10-cm depth leads to a normalized spectrum that is slightly lower at the period of 365 d compared with the normalized spectra obtained at 30 and 50 cm. The cross-wavelet spectrum can be computed from the wavelet transform of the two simultaneously sampled variables and is comparable with the covariance in ordinary correlation–regression analysis and the cross spectrum in Fourier analysis (Graf et al., 2014). The normalized real part of the cross wavelet spectrum is comparable with an R^2 value. Other than R^2 values obtained from conventional correlation analysis, it is localized in both the time and frequency domains. It indicates the maximum correlation after removing any potential phase shift (also called delay, which is the difference in timing of two consecutive maximal values of investigated signals) between the variables at this particular time and frequency (Graf et al., 2014). This phase shift is reported independently. Supplemental Material 3 provides a simple analysis of several artificial signals using wavelet coherence analysis to describe the concepts of perfect correlation, anticorrelation, and phase shift or phase angle, which is used below in the manuscript. We evaluated the phase shift between the SWC and ET_a time series using cross-wavelet analysis. The following equation is used to quantify the phase shift between a base signal (e.g., SWC) and a second signal (e.g., ET_a):

$$\text{Phase shift} = \text{Phase angle}/2\pi \times n \tag{9}$$

where phase shift (in days) and phase angle (in radians) refer to the difference in timing of two consecutive maximal values of the base and second signals (e.g., between the maxima of SWC and ET_a), and n represent the period (1/frequency) of the signals. The phase angle is quantified by wavelet coherence analysis through the cross-wavelet spectra.

In order to determine whether SWC controls ET_a or WSI or vice versa, we introduce the concept of "lag" defined as:

$$\begin{aligned} &\text{lag} = \text{Phase shift, if } -n/4 \le \text{ Phase shift } \le +n/4 \\ &\text{lag} = n/2 - |\text{Phase shift}|\,, \ \text{ if Phase shift} < -n/4 \\ &\text{lag } = \text{Phase shift} - n/2\,, \ \text{ if Phase shift} > +n/4 \end{aligned} \tag{10}$$

Negative lag values mean that the second signal controls the base signal (e.g., ET_a controls SWC), whereas positive lag values mean that the base signal controls the second one. Based on the above equation, abs(lag) values quantify the length of the time window for which a signal at time t is controlled by the status of the other signal during that time window, t − abs(lag).

In order to evaluate whether the reduction in yearly phase shift between ET_a and SWC is caused by a shift in ET_a or SWC (and/or both), cross-wavelet spectra were calculated between each of the signals and a benchmark signal with a constant frequency (365 d) and a constant phase (π/2). As a benchmark signal y, we used

$$y = \sin(2\pi t/365 + \pi/2) \tag{11}$$

The use of the above equation ensures the fluctuations of an imaginary signal at yearly cycle with a period of 365 d, and which has its maximal values at start of each period (first day of each period). Therefore, any phase shift occurring between

TABLE 1 ANOVA test to check the seasonality of the precipitation

Site	Mean ± SD				*F*	*p*
	Winter	Spring	Summer	Fall		
Energy-limited	252.0 ± 72.2	241.7 ± 73.6	278.1 ± 106.9	287.9 ± 43.0	0.53	.66
Water- limited	127.3 ± 52.9	157.5 ± 46.6	209.8 ± 89.1	170.6 ± 21. 5	2.45	.08
F	12.43	6.54	1.69	41.79		
p	.00	.03	.22	.00		

the benchmark signal and two other signals of ET_a and SWC quantifies the shift in ET_a and SWC signals.

In addition, in order to support the interpretation of the wavelet analyses, we carried out simple soil water balance simulations for a few scenarios. The simulations are used to show that precipitation might be an important control on the observed change in phase shift between ET_a and SWC. In each scenario, we assumed that the precipitation, P, is constant over time. This assumption is supported by an ANOVA analysis performed on the seasonal P data at both sites. At a .05 significance level, there is an observed seasonality at both sites (Table 1). The difference in P between both sites is mainly caused by higher winter and spring rainfall at the energy-limited site compared with the water-limited site.

We distinguished four scenarios each with a different yearly precipitation: 1,277.5, 1,095, 912.5, and 730 mm. These values span the ranges of precipitation amount observed at both sites. We also assumed that the annual fluctuations of ET_{crop} over time could be represented using a sine function:

$$ET_{crop}(t) = \langle ET_{crop}(t) \rangle \left[1 + \sin(2\pi t/365 + \pi/2)\right] \quad (12)$$

where $\langle ET_{crop} \rangle$ is the yearly averaged ET_{crop}.

Yearly averaged ET_{crop} was selected based on the observed values at the energy-limited and water-limited sites. The water balance model was a simple bucket model that assumed that the SWC could not exceed the water content at field capacity, and that excess water percolated rapidly out of the root zone. To model the reduction of evapotranspiration when the soil dried out, we used a reduction function that assumes a linear relation between the ratio of ET_a and ET_{crop} and the SWC, as is often applied in ecohydrological models or crop models (Allen et al., 1998).

We simulated the annual fluctuations of the SWC in the root zone for a period of 7 yr using the algorithms below. We simulated the water content in the root zone as

$$\begin{aligned} &\text{if} \quad SWC \le FC, \text{then} \\ &dSWC/dt = 1/L_{root}\left\{P - ET_a\left[ET_{crop}(t), SWC\right]\right\} \\ &\text{else} \quad dSWC/dt = 0 \end{aligned} \quad (13)$$

where FC is the water content at field capacity and L_{root} is the root zone depth. The ET_a is a function of the ET_{crop} and of the SWC:

$$\begin{aligned} &\text{if } SWC \le SWC_{crit}, \text{ then} \\ &ET_a = ET_{crop}\left(\frac{SWC - WP}{SWC_{crit} - WP}\right), \\ &\text{else } ET_a = ET_{crop} \end{aligned} \quad (14)$$

where SWC_{crit} is a critical water content below which ET_a decreases linearly by SWC, and WP is the SWC at WP at 15,000 hPa. We have listed the parameters used in the model in Table 2. The wavelet cross spectra were calculated between the simulated ET_a and the benchmark signal, as well as the simulated SWC and the benchmark signal.

TABLE 2 Parameters used in the simulation of the soil water balance. The notation *x*:*y*:*z* for the applied range of precipitation indicates that precipitation intensities from *x* to *z* were modeled in steps of *y*

Parameter[a]	Energy-limited site	Water-limited site
Applied range of precipitation, mm d^{-1}	2:0.5:3.5	1.25:0.5:2.75
FC, % (v/v)	29.8	29.8
WP, % (v/v)	8	8
Root depth, mm	500	500
SWC_{crit}	20	20
Avg. reference evapotranspiration, mm d^{-1}	1.964	2.299

[a]FC and WP, soil water content at field capacity and wilting point, respectively. SWC_{crit}, critical soil water content.

3 | RESULTS AND DISCUSSIONS

3.1 | Climatic and hydrological conditions at energy-limited and water-limited sites

We used the Budyko framework (Figure 2) to plot the yearly and 7-yr water balance of the energy-limited and water-limited sites for the period 2012–2018. For the 7-yr period, we assumed that the underlying assumption (zero change in

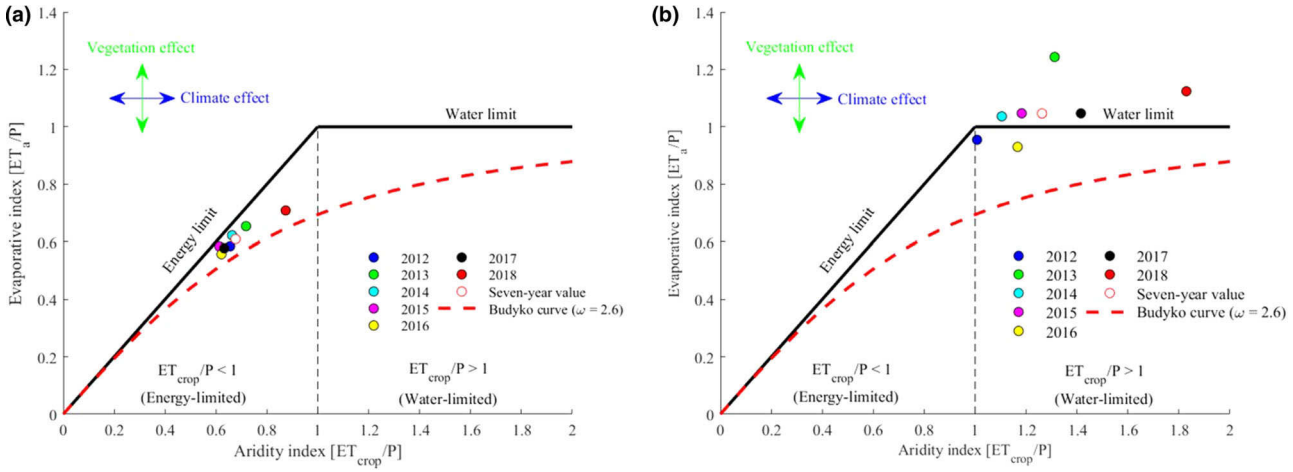

FIGURE 2 Budyko plots for (a) energy-limited and (b) water-limited sites during 2012–2018. The ω stands for free model parameter of Budyko function, ET_{crop} stands for crop height-adjusted evapotranspiration, and *P* stands for precipitation

TABLE 3 Yearly values of soil water balance components at both energy-limited and water-limited sites for the measurement period of 2012–2018

Year	*P*	ET_a	ET_{crop}	Capillary rise	Drainage	dSWS/d*t*	Net influx
	mm					mm yr^{-1}	mm
Energy-limited site							
2012	1,035.7	605.2	678.9	13.1	480.0	−36.4	−466.9
2013	982.3	642.4	705.3	26.1	425.7	−59.6	−399.5
2014	1,098.2	683.2	728.6	25.4	416.8	23.6	−391.3
2015	1,148.7	670.5	704.6	43.4	564.4	−42.8	−521.0
2016	1,102.7	614.4	685.6	38.0	526.8	−0.5	−488.7
2017	1,133.1	654.4	716.9	42.1	537.3	−16.4	−495.2
2018	917.6	650.2	801.9	42.1	375.9	−66.3	−333.8
Sum	7,418.3	4,520.3	5,021.9	230.3	3,326.8	−198.4	−3,096.4
Mean	1,059.8	645.8	717.4	32.9	475.3	−28.3	−44.2
SD	85.0	28.1	41.0	11.6	71.0	32.4	68.3
CV	8.0	4.4	5.7	35.1	14.9	114.5	15.4
Water-limited site							
2012	722.5	689.9	728.0	47.9	12.8	67.7	35.1
2013	588.0	731.0	771.5	107.8	87.3	−122.5	20.5
2014	710.9	736.8	785.3	133.3	45.2	62.2	88.1
2015	749.1	784.3	886.0	71.2	42.2	−6.3	29.0
2016	713.7	663.6	832.5	44.6	56.0	38.6	−11.4
2017	648.9	679.3	918.3	126.9	51.7	44.8	75.2
2018	523.4	588.1	957.3	82.5	62.4	−44.7	20.1
Sum	4,656.4	4,872.9	5,878.9	614.1	357.5	40.0	256.5
Mean	665.2	696.1	839.8	87.7	51.1	5.7	36.6
SD	82.3	62.8	83.9	36.0	22.5	69.2	34.2
CV	12.4	10.9	9.0	41.0	44.1	1211	93.5

Note. *P*, precipitation; ET_a, actual evapotranspiration; ET_{crop}, crop-height-adjusted reference evapotranspiration; dSWS/d*t*, the change in soil water storage over time; net influx, capillary rise minus drainage.

water storage) for the Budyko analysis is fulfilled, as the change in water storage in this period is 2.6% of the *P* at the energy-limited site and 0.8% of the *P* at the water-limited site (Table 3). At the energy-limited site, total P exceeds ET_a, leading to an EI of 0.58, whereas at the water-limited site, ET_a slightly exceeds *P*, resulting in an EI of 1.04. The aridity index (AI) for the 7-yr period is 0.66 for the energy-limited site and 1.26 at the water-limited site.

The yearly calculation of the Budyko values (Figure 2) shows a smaller variability at the energy-limited site compared with the water-limited site, indicating a larger climatic and hydrological variability at the water-limited site. Values of the different components of the soil water balance in Table 3 reflect this. The CV values of *P*, ET_{crop}, and ET_a are smaller at the energy-limited site compared with the water-limited site. The largest differences between the sites occur, however, for drainage and change in SWS. At the water-limited site, the yearly change in SWS ranges between −122.5 and 67.7 mm, and the yearly drainage ranges between 12.8 and 87.3 mm. These values occur in two consecutive years, namely 2012 and 2013. At the water-limited site, EI in 2013 and 2018 is >1 indicating the consumption of SWS by the vegetation and/or the net influx of water from upward capillary flow. There is a net influx of water through the bottom of the lysimeters. However, this net influx does not compensate for the *P* deficit in these years so that SWS change in both years is negative. The large ET_{crop} values and low rainfall in 2018 compared with the other years led to an increase in the aridity factor at the water-limited site, with a value of 1.83. The ET_{crop} was the largest value in the 7-yr period at 957.3 mm, whereas *P* was the lowest at only 523.4 mm.

Figure 3 shows SWC at three depths, ET_{crop}, and ET_a at the energy-limited and water-limited sites for the studied period. The results show that the mean wintertime (1 January–31 March) SWC{10 cm} values at the energy-limited site are higher (42.2 ± 2.2%) than at the water-limited site (35.5 ± 1.9%), as more rainfall water is available and ET_a is low for both locations. Differences in SWC during wintertime between both sites are less pronounced at deeper depths. The SWC{30 cm} is 37.1 ± 1.2% at the energy-limited site and 39.2 ± 0.6% at the water-limited site. At 50-cm depth, SWC is 36.6 ± 0.2 and 34.1 ± 1.8% for the energy-limited and water-limited sites, respectively.

After 2015, the minimal SWC during summer at the water-limited site decreases from an average of ∼22.6% to a value of ∼15%. At deeper depths, we observe no clear decline in the minimal SWC during summer over the different years. At the energy-limited site, minimal SWC decreases both in the surface layer and at 30-cm depth from 2015 on (Figure 3). Major controls are most likely the different climatic conditions, since soil, vegetation, and management are the same.

Figure 3 also shows that at the water-limited site, the rewetting of the soil profile in 2017 and 2018 occurs slower than that at the energy-limited site. This can be seen by comparing the SWC data of 2017 and 2018 between the summer and winter period at the energy-limited and water-limited sites. The change in SWC is much slower (the curves remain flat for longer) at the water-limited site Selhausen than at the energy-limited site.

Despite the fact that the soil profiles are rewetted in late summer, ET_a at the water-limited site does not increase. Based on the plant hydraulics, it can be assumed that the transpiration rate is linearly dependent on the difference between a weighted average of the soil water potentials in the root zone and the leaf water potential (Javaux, Couvreur, Vanderborght, & Vereecken, 2013). Assuming that the plants control the leaf water potential during stress periods and keep it constant when a critical leaf water potential is reached, ET_a should increase when the soil water potential increases during stress periods. However, we do not observe this at the water-limited site in 2017 and 2018. One possible explanation might be that the vegetation was not able to recover as soil was wetting, because the grass was slightly dried and brown and therefore did not transpire. If *P* is occurring during these times, a larger portion of it is partitioned into percolation and soil rewetting, and a smaller fraction than usual is routed into ET_a.

Figure 4 shows the global (time-averaged) power spectrum of ET_a, ET_{crop}, WSI, and SWC at the energy-limited and water-limited sites. Panel (a) presents the global power spectrum of ET_a and ET_{crop} at both sites showing uniquely centered signals at a period of 365 d (the yearly ET cycle). The strength of the ET_{crop} power in the yearly cycle is lower at the energy-limited site [918 $(mm\ d^{-1})^2$] compared with the water-limited site [1,188 $(mm\ d^{-1})^2$]. The ET_{crop} power in the yearly cycle [with mean value of 1,053 $(mm\ d^{-1})^2$] is considerably larger than the ET_a power [with mean 639 $(mm\ d^{-1})^2$] at both sites. The latter signal (ET_a) shows the opposite trend between the two sites, where its yearly power is higher at the energy-limited site [709 $(mm\ d^{-1})^2$] than at the water-limited site [569 $(mm\ d^{-1})^2$].

Panel (b) shows the global power spectrum of WSI vs. examined periods at both sites. The energy-limited site shows a weak global maximum at a period of 365 d with a power value of 1.03 $[(mm\ d^{-1})/(mm\ d^{-1})]^2$ that is more pronounced at the water-limited site with a power value of 2.12 $[(mm\ d^{-1})/(mm\ d^{-1})]^2$. This maximum corresponds to the drought stress that occurs during summer time.

Panels (c) and (d) of Figure 4 present the global power spectra of SWC at 10-, 30-, and 50-cm depths vs. the period of the measured signals at the energy-limited and water-limited sites, respectively. First, we see two dominant periods in the SWC signals at all depths and for both sites, with the strongest SWC signal occurring at 365 d and a second signal that is less strong occurring at 600 d. The power of the

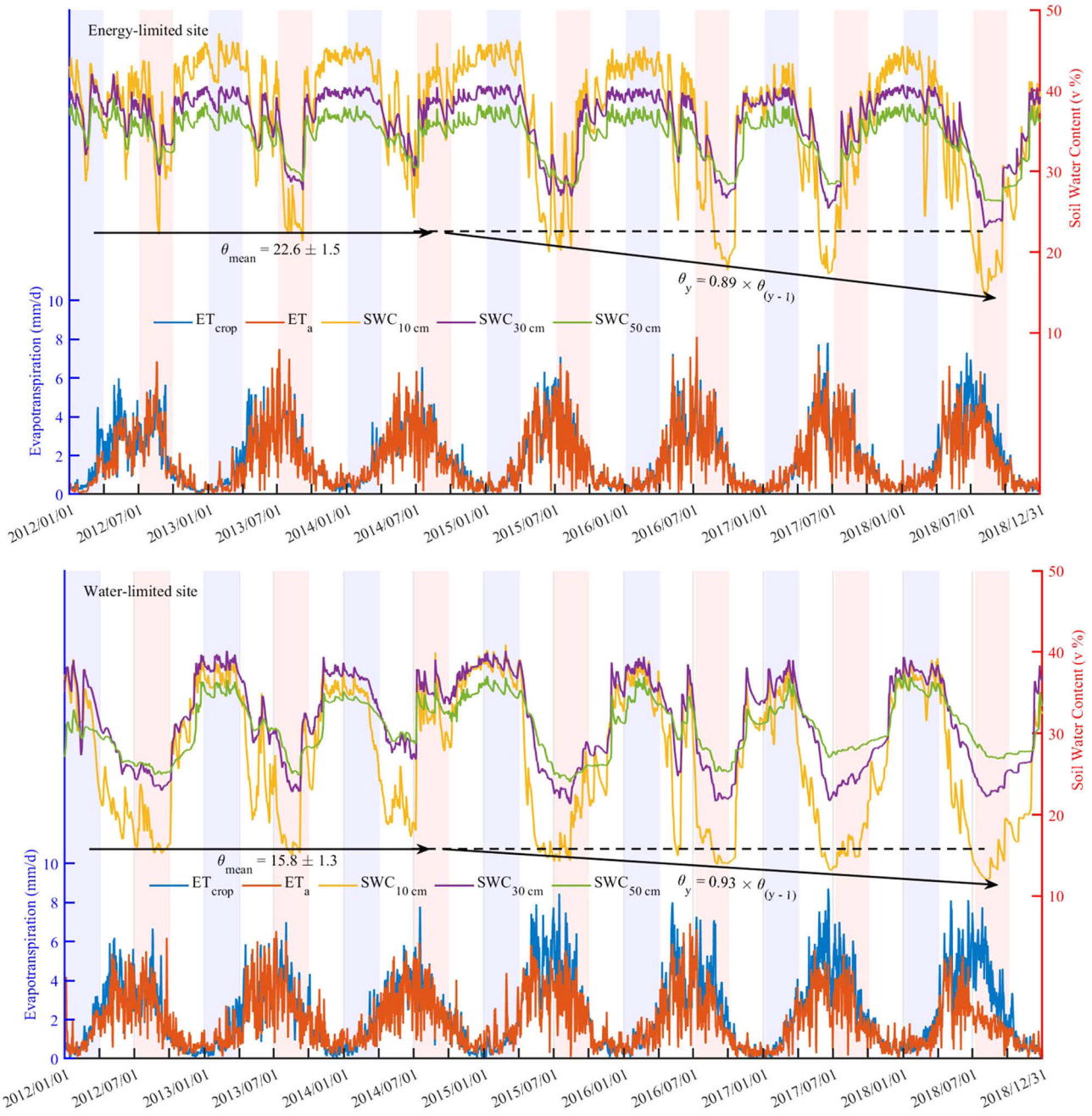

FIGURE 3 Time series data of daily actual (ET_a) and vegetation-height-adjusted reference (ET_{crop}) evapotranspiration, as well as soil water contents (SWC) at 10-, 30-, and 50-cm depths, of energy-limited and water-limited sites. The θ_{mean} stands for average of minimal SWC during different years, and θ_y and θ_{y-1} stand for minimum SWC values at given year of y and $y-1$, respectively

SWC signals at a period of 365 d is almost half (on average) that at the energy-limited site [with mean power values of 6,854(%)^2] compared with the water-limited site [with mean power values of 1,2576(%)^2], indicating the presence of stronger amplitudes in the SWC signal at the water-limited site. The strength of this signal is smaller for all depths at the energy-limited site than at the water-limited site. Panels (c) and (d) also show that the strength of the signal is depth dependent at both sites: the deeper the measurement level, the lower is the strength of the signal. At deeper depths, SWC is typically more stable due to less immediate meteorological effects.

Wavelet analysis also allows inspecting the time evolution of the power spectra for SWC, ET_a, ET_{crop}, and WSI. As already shown in Figure 3, we see an intensification of the SWC signal from 2015 onwards at the energy-limited site. This intensification of the SWC, caused by an increase in climatic forcing, which is stronger at the water-limited site than at the energy-limited site, occurs in all three depths but is less pronounced at deeper depths. We have illustrated this in

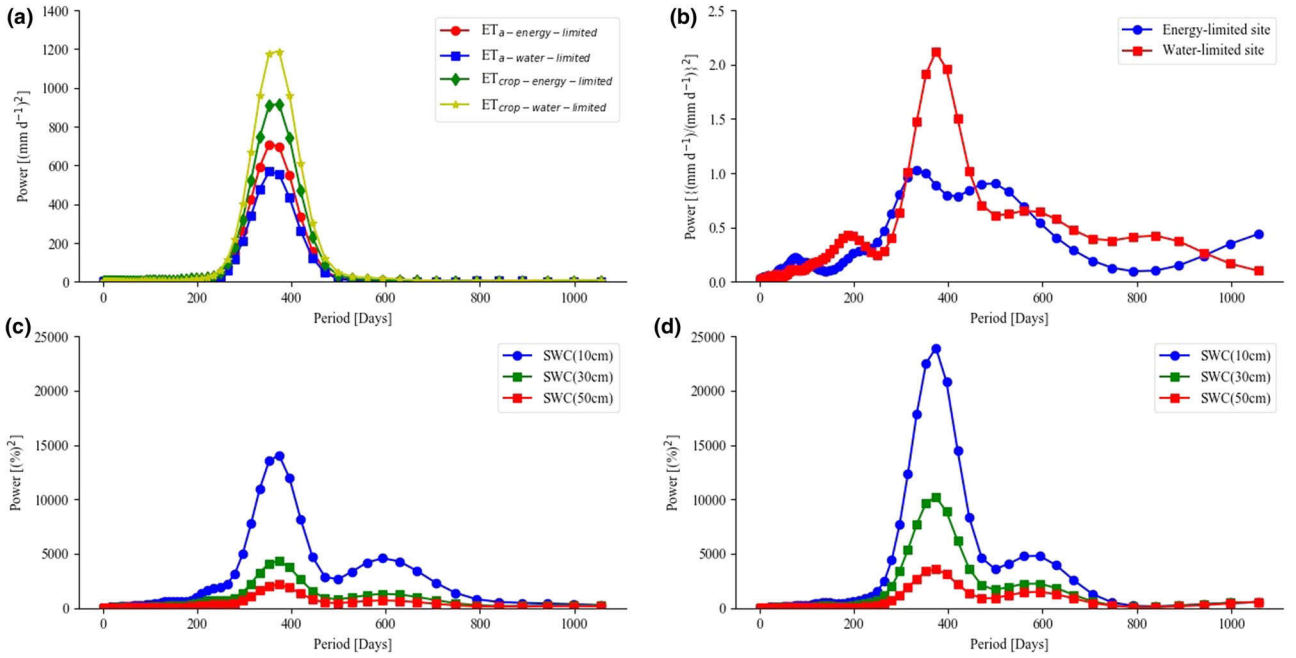

FIGURE 4 The global power spectra of (a) actual (ET_a) and vegetation-height-adjusted reference (ET_{crop}) evapotranspiration, (b) water stress index (WSI), and soil water content (SWC) at (c) energy-limited and (d) water-limited sites

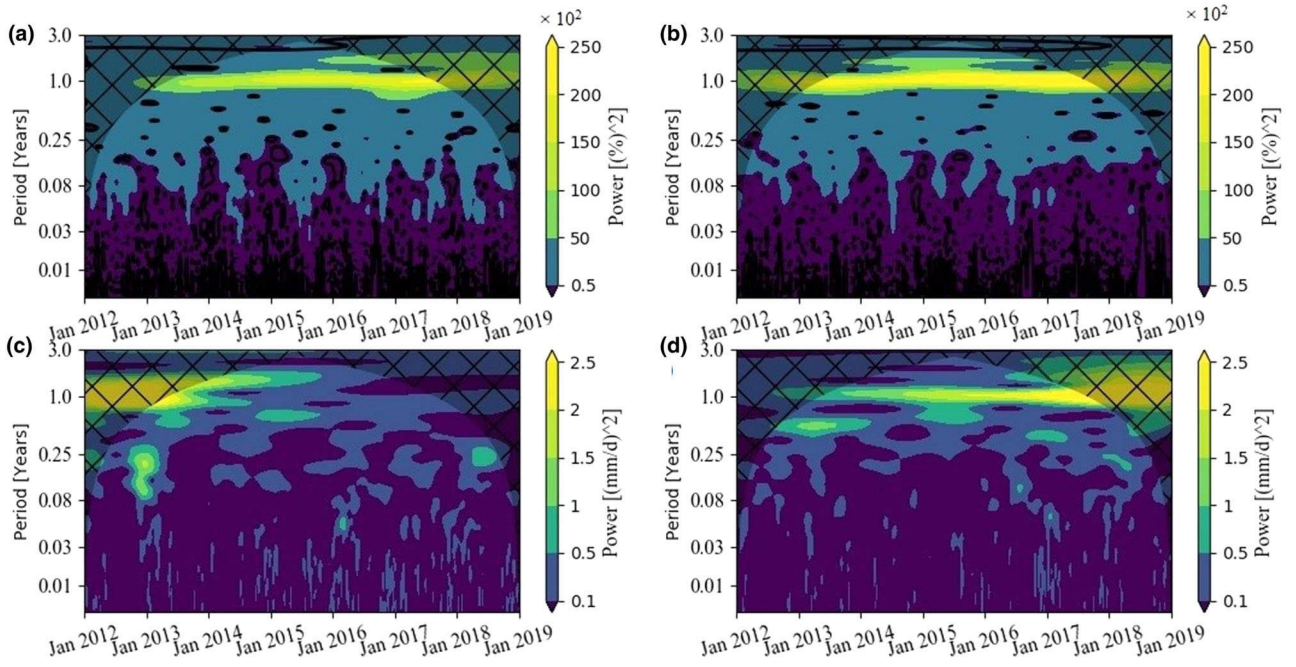

FIGURE 5 The power spectra of soil water content (SWC) at 10-cm depth at (a) energy-limited and (b) water-limited sites and water stress index (actual evapotranspiration [ET_a]/vegetation-height-adjusted reference evapotranspiration [ET_{crop}]) at (c) energy-limited and (d) water-limited sites

Figure 5 (Panels a and b), which shows the time and period variant power spectrum of SWC at 10 cm at the energy-limited and water-limited sites. We have presented the power spectrum maps of the SWC at other depths in Supplemental Material 4.

Although the power spectrum analysis of ET_{crop} and ET_a shows the constant strength of them at both sites for the measurement period (shown in Supplemental Material 4), there are decreasing and increasing intensities in the WSI over time at the energy-limited and water-limited sites,

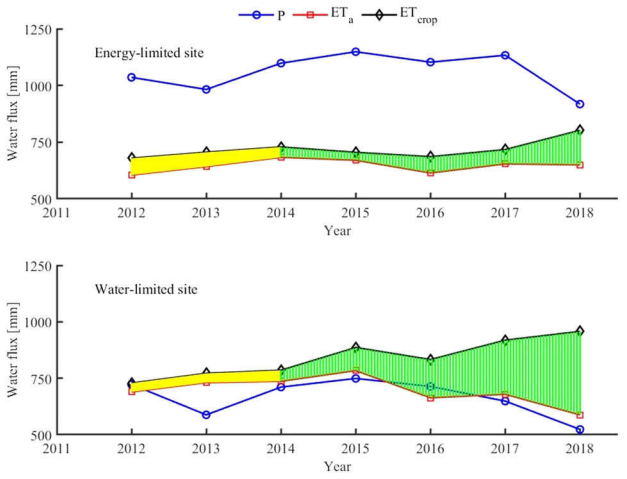

FIGURE 6 Distribution of actual (ET_a) and vegetation-height-adjusted reference (ET_{crop}) evapotranspiration and precipitation (P) at (a) energy-limited and (b) water-limited sites over different years. The shaded area shows the differences between ET_a and ET_{crop} values. Green = increasing trend, yellow = decreasing or a constant trend

respectively (Figure 5, Panels c and d). Intensity decreases at the energy-limited site because it becomes a more energy-limited site during 2014–2017, which is observable form the Budyko plot in Figure 2. The increase in intensity of WSI at the water-limited site seems to be related to the increasing drought intensity in this region. We report the results of power spectrum analysis on normalized signals in Supplemental Material 4.

The evolution of ET_{crop}, ET_a, and P from 2012 to 2018 for both sites is shown in Figure 6. At the water-limited site, the differences between ET_{crop} and ET_a remain constant in the first 3 yr. After 2014, the difference increases and reaches a maximum in 2018. At the energy-limited site, the difference is minimal in 2014 and increases over the next 4 yr to reach a maximum, but its value is much smaller compared with the water-limited site.

3.2 | Coherence between soil water content, evapotranspiration, and water stress index

We used wavelet coherence analysis to explore the relationship between SWC and ET_a or WSI for different times and frequencies. Since our analysis showed that the coherence between SWC{10 cm} and ET_a or between SWC{10 cm} and WSI is nearly identical for the other depths (30 and 50 cm), we present the detailed results for the first depth only, and for two other depths, we only report the averaged coherence values. The same applies to the coherence between total SWS in the profile and ET_a and/or between the SWS and WSI. Figures for SWC at 30 and 50 cm, as well as SWS, are reported in Supplemental Material 5.

The coherence between SWC and ET_a at all three depths at both sites is particularly strong at periods between 200 and 512 d (Figure 7a), suggesting a strong correlation between both signals at the annual cycle. The coherence between SWC and ET_a at other time cycles or periods (weekly, monthly, and/or seasonally) is unstable and erratic (Figures 7a and 7b).

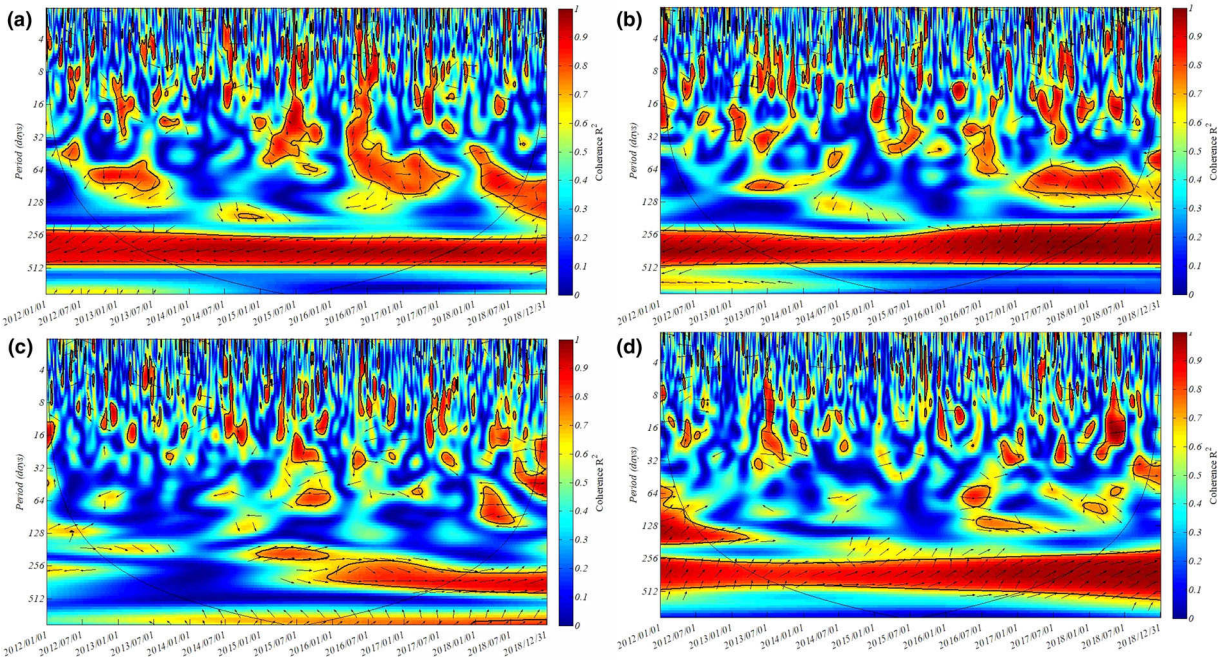

FIGURE 7 Wavelet coherence plots between average soil water content (SWC) at a depth of 10 cm (SWC{10 cm}) and actual evapotranspiration (ET_a) at (a) energy-limited and (b) water-limited sites and SWC{10 cm} and water stress index (WSI = ET_a/vegetation-height-adjusted reference evapotranspiration [ET_{crop}]) at (c) energy-limited and (d) water-limited sites

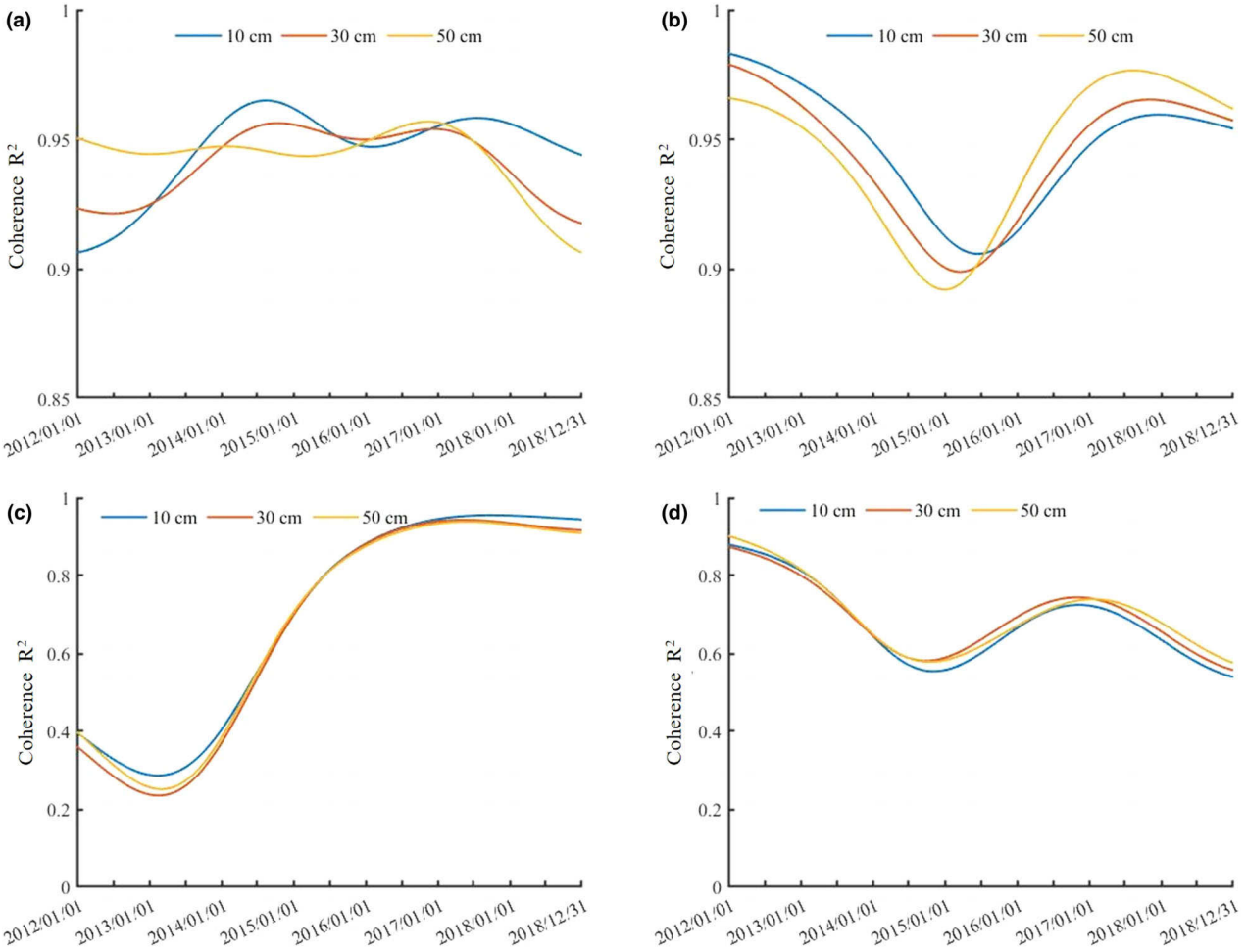

FIGURE 8 Coherence R^2 between average soil water content (SWC) at different depths of 10, 30, and 50 cm and actual evapotranspiration (ET_a) at (a) energy-limited and (b) water-limited sites and between SWC and ET_a/vegetation-height-adjusted reference evapotranspiration (ET_{crop}) at (c) energy-limited and (d) water-limited sites

Figure 7 also shows that the shorter the period, the higher the variation in coherence R^2 values. This can be explained by the fact that at shorter periods (daily to weekly), other environmental controls affect the SWC and ET_a relationship. At high frequencies, the coherence between SWC and ET_a observed at the yearly timescale gets lost because only factors determining ET_a are subject to fast changes (e.g., short-term fluctuations in rainfall, temperature, humidity, and the presence of cloudy days with low radiation). Soil water content, in contrast, changes slowly, especially during dry-down events, whereas rapid and strong changes are only possible after strong rain events.

The coherence between SWC and WSI shows a clearly different picture between the energy-limited and water-limited sites (Figure 7c and 7d). At the energy-limited site, high coherence values only occur in the middle of 2014 (change from blue to yellowish color). At the water-limited site, SWC and WSI remain highly correlated in the period of 2012–2018. This happens because any change in WSI index at the water-limited site will affect the status of the SWC and/or vice versa, and consequently a high correlation could be assumed between them for entire examined period. At the energy-limited site, in contrast, the variation in ET_a is mainly controlled by ET_a rather than SWC. Therefore, a low correlation between SWC and WSI is reasonable.

Figure 8 represents the evolution of the coherence between SWC at three depths and ET_a, as well as between SWC and WSI at the yearly cycle (365 d), showing a clear difference between the energy-limited and water-limited sites. Panel (a) of Figure 8 shows that at the energy-limited site, the yearly coherence between SWC and ET_a ranges between 0.9 and 0.97 for all depths and the full measurement period. Clearly, SWC and ET_a are highly correlated at this period that corresponds to the yearly cycle.

Panels (c) and (d) of Figure 8 show the evolution of the coherence of SWC and WSI at the energy-limited and water-limited sites, respectively. The energy-limited site shows an increase in the coherence over time, starting around the middle of 2014 and reaching a value of 1.0 at the beginning of 2017, indicating high correlation between SWC and the

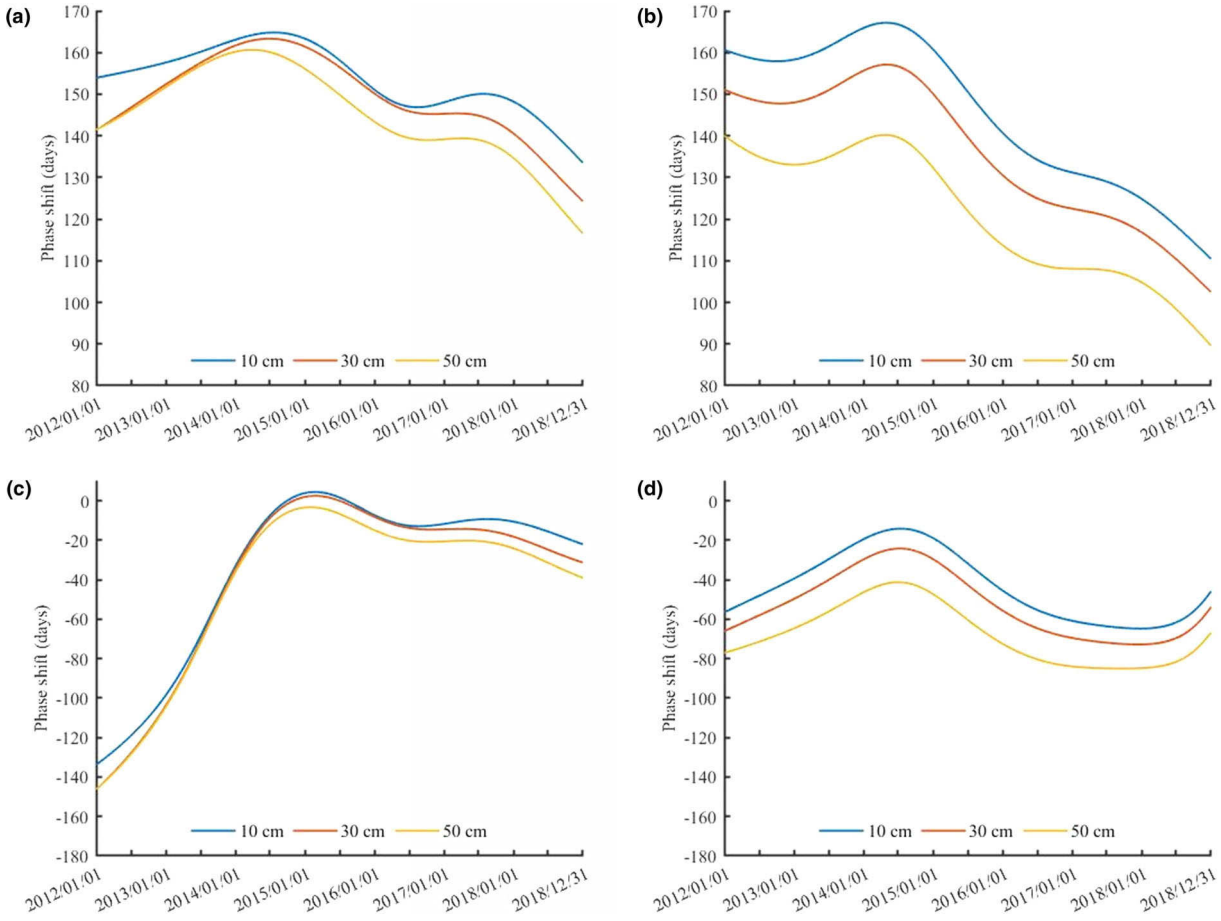

FIGURE 9 Phase shifts between soil water content (SWC) and actual evapotranspiration (ET_a) at (a) energy-limited and (b) water-limited sites and SWC and water stress index (WSI) at (c) energy-limited and (d) water-limited sites. We report the SWC at three different depths of 10, 30, and 50 cm

WSI. The phase shift (see discussion in Section 3.3) shows SWC and WSI to be fully in phase with a positive correlation indicating that a high value of ET_a/ET_{crop} occurs when SWC in the profile is high. In contrast, at the water-limited site, the coherence decreases from 0.9 down to 0.6 at the end of the measurement period, indicating a weakening correlation between SWC and WSI. Around the beginning of 2015, the coherence already fell to its minimum value of 0.6, but increased to a maximum of 0.75 in the beginning of 2017.

3.3 | Phase shift analysis between soil water content, evapotranspiration, and water stress index

The wavelet coherence analysis allows analyzing the phase shifts between SWC and ET_a and between SWC and WSI. The arrows in Figure 7 indicate the phase shifts. More explanation on the meaning of arrow directions is provided in Supplemental Material 3. The direction of the arrows (mostly left aligned) in Panels (a) and (b) of Figure 7 indicates an anti-correlation between SWC (depth-independently) and ET_a at a yearly cycle at both sites. Perfect left-aligned arrows mean that the examined variables lag behind each other with a phase shift of, in the case of an annual cycle, 6 mo. However, inspection of the arrow direction in the yearly cycle in Panels (a) and (b) of Figure 7 shows nearly identical left-aligned arrows in 2014. Before or after 2014, arrows point downward for the SWC–CET_a relations and upward for the SWC–WSI relation, indicating that ET_a is lagging behind SWC and SWC is lagging behind WSI. In general, downward arrows indicate positive (second variable lags) phase shifts and upward arrows negative (first variable lags) phase shifts. Figure 9 shows the annual-period phase shifts for SWC–ET_a (Panels a and b) and SWC–WSI (Panels c and d) over time for the energy-limited and water-limited sites, respectively. For a more intuitive interpretation, we converted the phase angles in radians to phase shifts in days.

Panel (a) of Figure 9 shows phase shifts between SWC and ET_a at the energy-limited site. We observe a positive phase shift between SWC and ET_a, indicating that ET_a is lagging behind the SWC. The phase shift between SWC and ET_a at

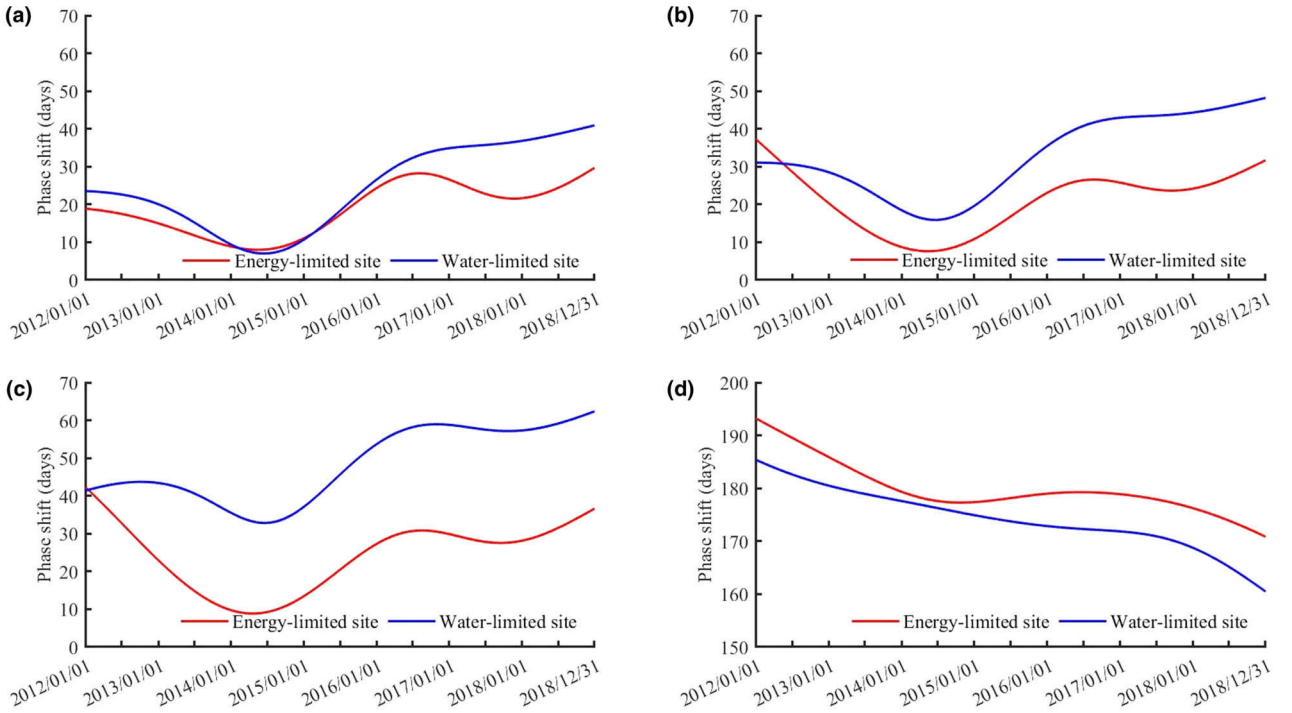

FIGURE 10 Yearly phase shifts between the benchmark signal (y) and soil water content (SWC) at different depths of (a) 10, (b) 30, and (c) 50 cm and (d) actual evapotranspiration (ET_a) over energy-limited and water-limited sites

the energy-limited site reaches a maximum of ∼160 d (i.e., the maximum of the ET_a occurs 160 d later than the maximum of SWC, or the minimum of SWC occurs 183 − 160 = 23 d later than the maximum ET_a) around the middle of 2014, and this is the case for all depths. This means that the rate of ET_a occurring during the previous 23 d (t − 23) is influencing SWC at time t. After the middle of 2014, the phase shifts decrease up to the end of the measurement period (2018), with values ranging between 140 and 115 d being equal to lag times of −43 and −68 d. This means that by advancing in time from the middle of 2014 toward 2018, the time window in which ET_a controls SWC is longer than before. We also observe that the differences between the maximum values and the final values are in the same range, indicating that the change in phase shift over time is depth independent.

Panel (b) of Figure 9 shows that the phase shift between ET_a and SWC at the water-limited site obtains its maximum in the middle of 2014, and this is for all depths. This finding corresponds to the observations at the energy-limited site. In addition, changes in phase shift from the middle of 2014 to the end of 2018 are almost identical for the three depths. We also observed this at the energy-limited site. Two things are fundamentally different, however. First, the decrease in phase shifts after the middle of 2014 is much stronger than at the energy-limited site, indicating that water stress also occurs at larger depths. Second, the absolute differences in phase shifts between depths are more pronounced.

Panel (c) of Figure 9 shows the phase shifts between SWC and WSI at the energy-limited site. The phase shift between SWC and WSI at the energy-limited site reaches a maximum of zero at the middle of 2014 for the first two depths. The deepest layer shows a slightly negative value at this time. This means that SWC and WSI are perfectly to almost perfectly in phase and are positively correlated. We can explain this by the fact that high SWC values lead to ET_a values being equal to ET_{crop}, a situation typically occurring in wintertime. Before or after 2014, any increase in soil dryness causes negative phase shifts between SWC and WSI, indicating that SWC is lagging behind the WSI. This means that WSI controls SWC by a lag time of <40 d. The interesting thing at the energy-limited site is that before 2014, SWC controlled WSI, whereas after mid-2014, WSI started controlling SWC.

Panel (d) of Figure 9 shows the phase shift between SWC and WSI at the water-limited site for three depths. The maximum phase shift occurs in the middle of 2014, but it is lower than zero and depth dependent. This is what we have also observed at the energy-limited site. The negative phase shifts after the middle of 2014 until 2018 indicate that the summer minimum of WSI occurs before the one of SWC. The presence of water stress at the water-limited site leads also to larger negative phase shifts than at the energy-limited site after the middle of 2014. This means that towards 2018, WSI starts controlling SWC by a lag time of ∼60 d in the surface soil and 90 d in the deeper layer (which is longer than the lag times at the

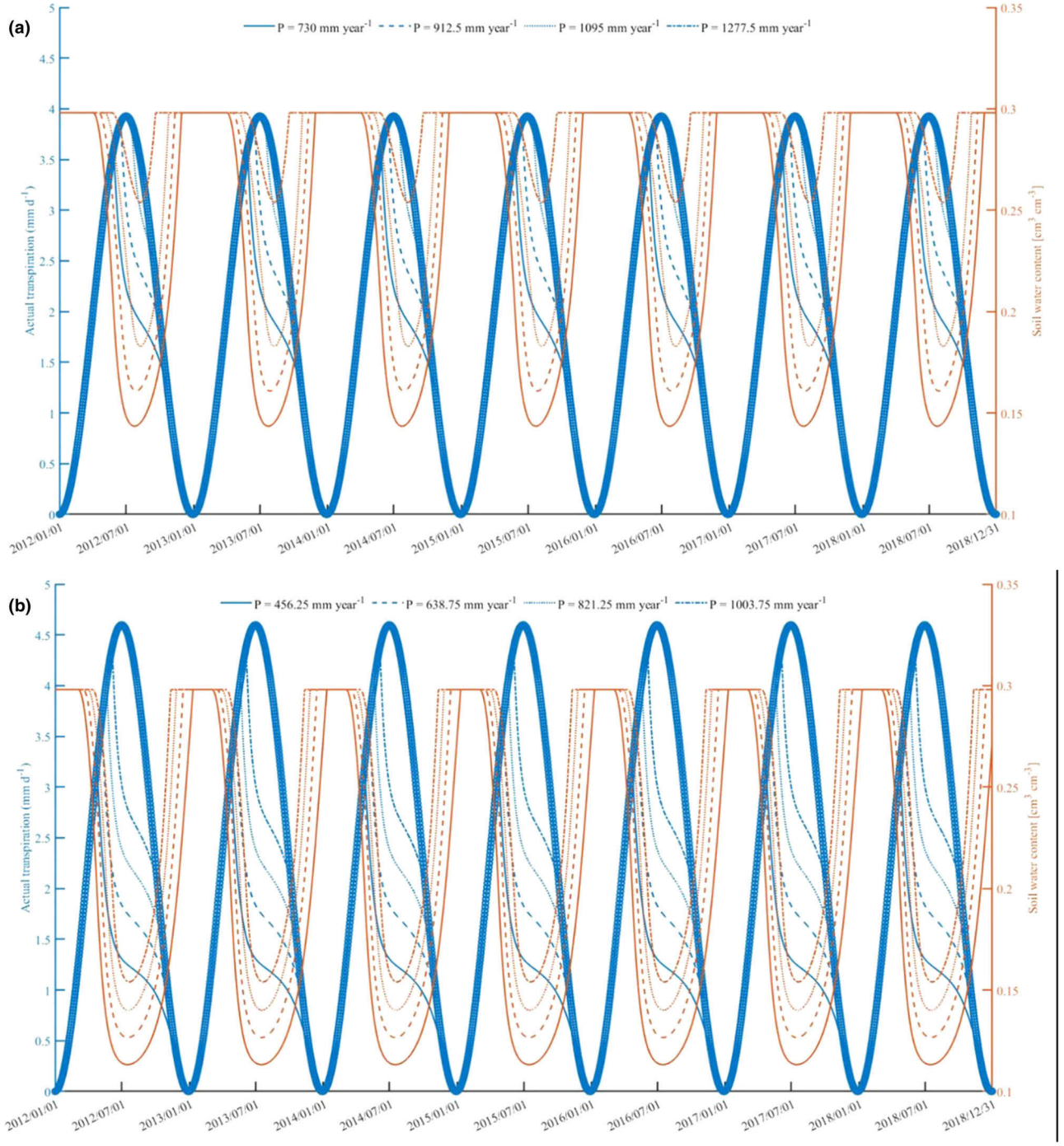

FIGURE 11 Evolution of simulated actual evapotranspiration (ET_a) and soil water content (SWC) by a simple model at (a) energy-limited and (b) water-limited sites. The *P* values indicate precipitation

energy-limited site, which showed a lag time of <40 d), demonstrating the effect of higher dryness on the control of WSI on SWC.

There can be three reasons for the change in phase shift between SWC and ET_a over the years. First, the maximum SWC occurs later in winter because the soil was drier than usual (e.g., dry autumn or early winter) and requires more time to wet again. Second, maximum ET_a occurs earlier in the season (late spring or early summer) because the soil water stock is depleted earlier due to the small amount of water stored in the soil after winter and/or because there is less *P* in spring and summer. Third, a combination of the two previous cases is possible. Finally, changes in rooting depth and root mass, as well as changes in species composition and grass canopy, due to the translocation from an energy- to a water-limited site might theoretically affect coherence and phase shift between

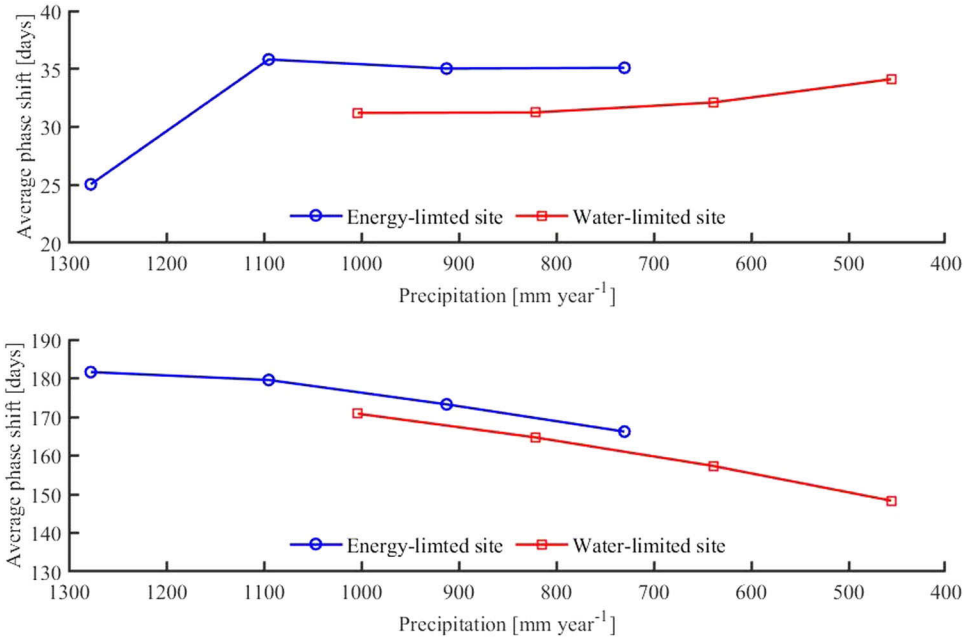

FIGURE 12 The average (over both time and period) phase shift (a) between benchmark signal *y* and simulated soil water content and (b) between benchmark signal and simulated actual evapotranspiration at energy-limited and water-limited sites

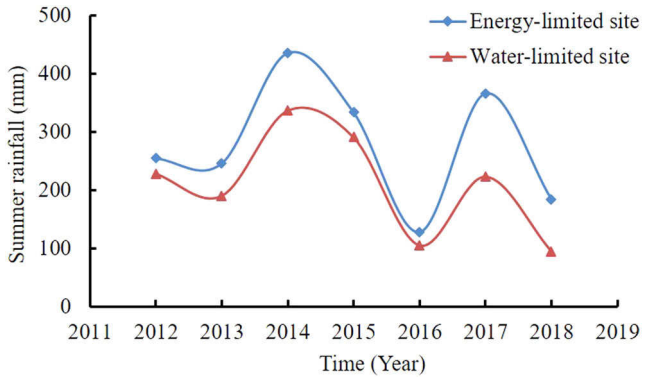

FIGURE 13 Summertime (1 July–30 September) rainfall occurring in different years at energy-limited and water-limited sites

SWC and ET_a. However, no data were available to test this explanation.

In order to check which of these three cases caused the phase shift, we created a benchmark signal (*y*, see Equation 9), which reaches its maximum at the beginning of the year and its minimum in the middle of the year. Then, the phase shift is examined between *y* and SWC, as well as ET_a. We show the results in Figure 10 for both the energy-limited and water-limited sites.

The phase shift between the benchmark signal and SWC is generally smaller in the energy-limited site than in the water-limited site and increases with depth (Figures 10a–10c). The phase shift of 10–40 d for the energy-limited site indicates that the annual SWC reach their maxima around 10–40 d after the start of the year. In the drier climate of the water-limited site, this phase shift ranges between 10 and 60 d and is larger for deeper soil layers. We can explain the increase of phase shift with depth by the delay of soil rewetting when ET_a starts to decrease due to water infiltrating from the top surface. The smaller precipitation at the water-limited site leads to a slower rewetting and hence a larger phase shift between the benchmark signal and SWC. Looking at the evolution of the phase shift over time, a minimal phase shift between the benchmark signal and the SWC occurs around mid-2014 at both locations. As the drying becomes stronger after 2015, the phase shift increases at both sites, indicating that the observed SWC signal is occurring later in the year.

Panel (d) of Figure 10 shows a consistent shift of the ET_a maxima towards earlier in the season (by ~20 d at the energy-limited site and ~25 d at the water-limited site) during the measurement period. As a conclusion, at both sites, the occurrence of maximal ET_a is shifted to earlier times, whereas the maximal SWC is shifted to later times, and these shifts are more pronounced at the drier site (water-limited site). However, the shift in maximum SWC is much more pronounced than the shift in maximum ET_a. The net effect of these shifts at both sites leads to a decrease in the phase shift between the SWC and ET_a signals, as observed from the phase shift analysis between SWC and ET_a (Figure 9).

In order to evaluate whether the changes in the SWC and ET_a signals, and their change in phase shift against the reference signal, can be explained by changes in annual precipitation at both sites using a simple water balance model, we analyzed the simulated SWC and ET_a for both sites for a range of yearly precipitation rates (Figure 11). We show the

simulated SWC and ET_a for both sites for a range of yearly precipitation rates in Figure 11. We also present the average phase shift (over both period and time) between the benchmark signal and the simulated SWC and ET_a in Figure 12 vs. the simulated annual precipitation rate. These simulations show how phase shift increases with decreasing precipitation. The time when the maximal SWC is reached moves from early January to late January or early February. However, the phase shifts of the simulated ET_a with respect to the benchmark signal are similar to the observed ones. The phase shifts of the simulated ET_a with respect to the reference signal are similar to the observed ones. They show the same difference between the sites and a similar change in function of changing precipitation. In the case of SWC, the simulated phase shifts do not vary so strongly with annual precipitation as the measured one. However, the change of the phase shift with precipitation is qualitatively the same with larger phase shifts for smaller precipitation. The reason for this difference between observed and simulated SWC phase shifts could be the constant SWC (i.e. equal to SWC at field capacity [SWC_{FC}]) during the winter period.

The fact that 2014 appears to be a turning point with respect to the impact on the phase shift between SWC and ET_a and between SWC and WSI is related to the presence of wetter summer conditions, with high rainfall amounts compared with earlier and later years (Figure 13).

4 | SUMMARY AND CONCLUSIONS

The relationship between SWC and ET_a at water-limited and energy-limited sites under grassland in Germany was investigated for the observation period of 2012–2018. We used nine weighable lysimeters to quantify all terms of the soil water balance. In addition, we performed SWC measurements at three depths. From the nine lysimeters, three lysimeters were translocated from the Rollesbroich (energy-limited) to the Selhausen (water-limited) site. The observation period between 2012 and 2018 provided daily values of the soil water balance. We applied continuous wavelet transform to investigate the power spectrum, the coherence, and the phase shift between SWC, ET_a, and the WSI (defined as the ratio between ET_a and ET_{crop}). Power spectrum analysis showed a strong power of all signals (ET_a, ET_{crop}, WSI, and SWC) in the yearly cycle at both sites. The ET_{crop} and WSI both had a higher power in the annual period at the water-limited site than at the energy-limited site, indicating the higher water stress at the water-limited site. Contrary to ET_a and ET_{crop}, which showed a unimodal power spectrum, the SWC signals showed a bimodal power spectrum centered on periods of around 365 and 600 d. The power in the annual cycle was particularly visible at the water-limited site. The strength of the SWC signals was depth dependent at both sites, with signal strength decreasing with soil depth. A key finding of this paper is the presence of a decreasing trend in the phase shift between SWC and ET_a, and an increasing phase shift between SWC and WSI. This was derived from a wavelet coherence analysis. At both sites, the change in phase shift started in 2014 after a wet summer (Ionita et al., 2017; Orth, Zscheischler, & Seneviratne, 2016). The decrease in phase shift between SWC and ET_a at both sites was caused by a shift in maximum ET_a towards earlier times in the summer season and a shift in the SWC towards later times in the winter season. The observed phase shifts between SWC and ET_a and between SWC and WSI were depth dependent, especially at the water-limited site. The change in phase shift between both sets (SWC–ET_a and SWC–WSI) indicated that the lag time between SWC and ET_a and between SWC and WSI were increasing. Therefore, the more negative lag values obtained between both sets (SWC–ET_a and SWC–WSI) showed that the duration of the time that ET_a and WSI control SWC was increasing as we approached 2018. Using a conceptual model, we demonstrate that the increasingly dry conditions from 2014 onwards are likely the reason for the change in phase shift over time. The extremely dry year of 2018 increased the aridity index at both the water- and energy-limited sites. At the energy-limited site, we observed an increase in the EI, whereas at the water-limited site, the EI =1 for all years. Finally, we noticed a change in phase shift between SWC and ET_a due to the occurrence of increasing drought in a grassland. The maximum of ET_a occurs earlier as dry conditions prevail over the years. This might have implications for the management of grasslands in terms of the amount and timing of fertilizer application and the timing and number of cutting periods. This effect might become more severe as climate change proceeds and droughts become more frequent. Most likely, this phenomenon of change in phase shift may also be relevant for cropped systems. The other interesting finding is that when ET_a is reduced due to drought, an increase in SWC towards the end of the growing season is not followed by an increase in evapotranspiration. We would expect such an increase when we assume that under stress conditions, the water potential in the leaves is regulated by stomata and kept at constant value (isohydric plants). Using plant hydraulics to calculate the water flow through the plant from the soil to the leaves based on the difference between the soil and the leaf water potential should lead to a higher water flow when the soil water potential increases. A further decrease in transpiration when the soil is rewetted after a dry period indicates that either the plant hydraulic conductance is further declining during this wetting phase and/or the leaf water potential is increasing more strongly than the soil water potential. During droughts, the grass leaves die off and the grass surface turns brown. Such a die off suggests a decrease in plant hydraulic conductance. A stronger increase in leaf water potential with increasing soil water potential would imply a hysteretic relation between

stomatal conductance and leaf water potential. This behavior is not captured well by most root water uptake models. More detailed studies on the impact of dryness and drought on the rooting system and canopy composition of the grass cover might be helpful in better understanding the observed changes in coherence and phase shifts between SWC and ET_a. Further studies are needed at larger scales and including different soil systems, climate, and vegetation regimes to assess the generality of the observed phase shift during longer periods of water stress and climate-relevant timescales.

ACKNOWLEDGMENTS

Authors thank the German Federal Ministry of Education and Research (BMBF) for financing the lysimeter network TERENO SoilCan and TERENO for providing the data. The contribution of A.G. was supported by BMBF Project 01LN1313A. M.R. is thankful for the cooperation from International & Scientific Cooperation Office of University of Maragheh. M.R. gratefully acknowledges the support received from Forschungszentrum Jülich.

CONFLICT OF INTEREST

The authors declare no conflict of interest.

ORCID

Mehdi Rahmati https://orcid.org/0000-0001-5547-6442
Jannis Groh https://orcid.org/0000-0002-1681-2850
Alexander Graf https://orcid.org/0000-0003-4870-7622
Thomas Pütz https://orcid.org/0000-0003-2101-448X
Jan Vanderborght https://orcid.org/0000-0001-7381-3211
Harry Vereecken https://orcid.org/0000-0002-8051-8517

REFERENCES

Allen, R. G., Pereira, L. S., Raes, D., & Smith, M. (1998). *Crop evapotranspiration-Guidelines for computing crop water requirements*. Rome: FAO.

Beckers, J.-M., & Rixen, M. (2003). EOF calculations and data filling from incomplete oceanographic datasets. *Journal of Atmospheric and oceanic technology*, *20*, 1839–1856. https://doi.org/10.1175/1520-0426(2003)020⟨1839:ECADFF⟩2.0.CO;2

Bogena, H., Montzka, C., Huisman, J., Graf, A., Schmidt, M., Stockinger, M., … Vereecken, H. (2018). The TERENO-rur hydrological observatory: A multiscale multi-compartment research platform for the advancement of hydrological science. *Vadose Zone Journal*, *17*(1). https://doi.org/10.2136/vzj2018.03.0055

Budyko, M. I. (1958). *The heat balance of the earth's surface*. Washington DC: U.S. Department of Commerce.

Budyko, M. I., & Miller, D. H. (1974). *Climate and life*. New York: Academic Press.

Eden, U. (2012). *Drought assessment by evapotranspiration mapping in Twente, the Netherlands* (Master's thesis). Twente, the Netherlands: University of Twente.

Feng, X., Porporato, A., & Rodriguez-Iturbe, I. (2015). Stochastic soil water balance under seasonal climates. *Proceedings of the Royal Society A: Mathematical, Physical and Engineering Sciences*, *471*(2174). https://doi.org/10.1098/rspa.2014.0623

Graf, A. (2017). Gap-filling meteorological variables with empirical orthogonal functions. In *Proceedings from the 2017 EGU General Assembly* (p. 8491). Munich, Germany: European Geosciences Union.

Graf, A., Bogena, H. R., Drüe, C., Hardelauf, H., Pütz, T., Heinemann, G., & Vereecken, H. (2014). Spatiotemporal relations between water budget components and soil water content in a forested tributary catchment. *Water Resources Research*, *50*, 4837–4857. https://doi.org/10.1002/2013WR014516

Grinsted, A., Moore, J. C., & Jevrejeva, S. (2004). Application of the cross wavelet transform and wavelet coherence to geophysical time series. *Nonlinear Processes In Geophysics*, *11*, 561–566. https://doi.org/10.5194/npg-11-561-2004

Groh, J., Pütz, T., Gerke, H., Vanderborght, J., & Vereecken, H. (2019). Quantification and prediction of nighttime evapotranspiration for two distinct grassland ecosystems. *Water Resources Research*, *55*, 2961–2975.

Groh, J., Slawitsch, V., Herndl, M., Graf, A., Vereecken, H., & Pütz, T. (2018). Determining dew and hoar frost formation for a low mountain range and alpine grassland site by weighable lysimeter. *Journal of Hydrology*, *563*, 372–381.

Groh, J., Vanderborght, J., Pütz, T., & Vereecken, H. (2016). How to control the lysimeter bottom boundary to investigate the effect of climate change on soil processes? *Vadose Zone Journal*, *15*(7). https://doi.org/10.2136/vzj2015.08.0113

Groh, J., Vanderborght, J., Pütz, T., Vogel, H.-J., Gründling, R., Rupp, H., … Gerke, Horst H. (2020). Responses of soil water storage and crop water use efficiency to changing climatic conditions: A lysimeter-based space-for-time approach. *Hydrology and Earth System Sciences*, *24*, 1211–1225. https://doi.org/10.5194/hess-24-1211-2020

Hecht-Nielsen, R. (1990). *Neurocomputing*. Boston, MA: Addison-Wesley Publishing Company.

Javaux, M., Couvreur, V., Vanderborght, J., & Vereecken, H. (2013). Root water uptake: From three-dimensional biophysical processes to macroscopic modeling approaches. *Vadose Zone Journal*, *12*(4). https://doi.org/10.2136/vzj2013.02.0042

Ionita, M., Tallaksen, L., Kingston, D., Stagge, J., Laaha, G., Van Lanen, H., … Haslinger, H. (2017). The European 2015 drought from a climatological perspective. *Hydrology and Earth System Sciences*, *21*, 1397–1419. https://doi.org/10.5194/hess-21-1397-2017

Jung, M., Reichstein, M., Ciais, P., Seneviratne, S. I., Sheffield, J., Goulden, M. L., … Zhang, K. (2010). Recent decline in the global land evapotranspiration trend due to limited moisture supply. *Nature*, *467*, 951. https://doi.org/10.1038/nature09396

Küpper, W., Groh, J., Fürst, L., Meulendick, P., Vereecken, H., & Pütz, T. (2017). TERENO-SOILCan: Management eines deutschlandweiten Lysimeternetzwerkes. In *Gumpensteiner Lysimetertagung: Lysimeterforschung - Möglichkeiten und Grenzen* (pp. 175–180). Irdning, Austria: Höhere Bundeslehr- und Forschungsanstalt für Landwirtschaft Raumberg-Gumpenstein.

Li, S., Liang, W., Zhang, W., & Liu, Q. (2016). Response of soil moisture to hydro-meteorological variables under different precipitation gradients in the Yellow River basin. *Water Resources Management*, *30*, 1867–1884. https://doi.org/10.1007/s11269-016-1244-7

McColl, K. A., He, Q., Lu, H., & Entekhabi, D. (2019). Short-term and long-term surface soil moisture memory time scales are spatially

anticorrelated at global scales. *Journal of Hydrometeorology*, *20*, 1165–1182. https://doi.org/10.1175/JHM-D-18-0141.1

Miralles, D. G., Gentine, P., Seneviratne, S. I., & Teuling, A. J. (2019). Land–atmospheric feedbacks during droughts and heatwaves: State of the science and current challenges. *Annals of the New York Academy of Sciences*, *1436*, 19–35. https://doi.org/10.1111/nyas.13912

Moran, M. S., Peters-Lidard, C. D., Watts, J. M., & McElroy, S. (2004). Estimating soil moisture at the watershed scale with satellite-based radar and land surface models. *Canadian Journal of Remote Sensing*, *30*, 805–826.

Orth, R. (2013). *Persistence of soil moisture: Controls, associated predictability and implications for land surface climate* (Doctoral dissertation). Zürich: ETH Zürich.

Orth, R., & Seneviratne, S. I. (2013). Propagation of soil moisture memory to streamflow and evapotranspiration in Europe. *Hydrology and Earth System Sciences*, *17*, 3895–3911. https://doi.org/10.5194/hess-17-3895-2013

Orth, R., Zscheischler, J., & Seneviratne, S. I. (2016). Record dry summer in 2015 challenges precipitation projections in Central Europe. *Scientific Reports*, *6*. https://doi.org/10.1038/srep28334

Pachepsky, Y. A., & Rawls, W. (1999). Accuracy and reliability of pedotransfer functions as affected by grouping soils. *Soil Science Society of America Journal*, *63*, 1748–1757. https://doi.org/10.2136/sssaj1999.6361748x

Peters, A., Groh, J., Schrader, F., Durner, W., Vereecken, H., & Pütz, T. (2017). Towards an unbiased filter routine to determine precipitation and evapotranspiration from high precision lysimeter measurements. *Journal of Hydrology*, *549*, 731–740. https://doi.org/10.1016/j.jhydrol.2017.04.015

Pütz, T., Kiese, R., Wollschläger, U., Groh, J., Rupp, H., Zacharias, S., … Vereecken, H. (2016). TERENO-SOILCan: A lysimeter-network in Germany observing soil processes and plant diversity influenced by climate change. *Environmental Earth Sciences*, *75*, 1242. https://doi.org/10.1007/s12665-016-6031-5

Rahmati, M. (2017). Reliable and accurate point-based prediction of cumulative infiltration using soil readily available characteristics: A comparison between GMDH, ANN, and MLR. *Journal of Hydrology*, *551*, 81–91. https://doi.org/10.1016/j.jhydrol.2017.05.046

Robinson, D., Campbell, C., Hopmans, J., Hornbuckle, B. K., Jones, S. B., Knight, R., … Wendroth, O. (2008). Soil moisture measurement for ecological and hydrological watershed-scale observatories: A review. *Vadose Zone Journal*, *7*, 358–389. https://doi.org/10.2136/vzj2007.0143

Scanlon, B. R., Keese, K. E., Flint, A. L., Flint, L. E., Gaye, C. B., Edmunds, W. M., … Simmers, I. (2006). Global synthesis of groundwater recharge in semiarid and arid regions. *Hydrological Processes*, *20*, 3335–3370. https://doi.org/10.1002/hyp.6335

Seneviratne, S. I., Corti, T., Davin, E. L., Hirschi, M., Jaeger, E. B., Lehner, I., … Teuling, Adriaan J. (2010). Investigating soil moisture–climate interactions in a changing climate: A review. *Earth-Science Reviews*, *99*, 125–161. https://doi.org/10.1016/j.earscirev.2010.02.004

Si, B. C. (2008). Spatial scaling analyses of soil physical properties: A review of spectral and wavelet methods. *Vadose Zone Journal*, *7*, 547–562. https://doi.org/10.2136/vzj2007.0040

Speich, M. J. (2019). Quantifying and modeling water availability in temperate forests: A review of drought and aridity indices. *iForest-Biogeosciences and Forestry*, *12*, 1–16. https://doi.org/10.3832/ifor2934-011

Teuling, A. J., Hirschi, M., Ohmura, A., Wild, M., Reichstein, M., Ciais, P., … Seneviratne, S. I. (2009). A regional perspective on trends in continental evaporation. *Geophysical Research Letters*, *36*(2). https://doi.org/10.1029/2008gl036584

Torrence, C., & Compo, G. P. (1998). A practical guide to wavelet analysis. *Bulletin of the American Meteorological society*, *79*, 61–78. https://doi.org/10.1175/1520-0477(1998)079⟨0061:APGTWA⟩2.0.CO;2

Wang, K., & Dickinson, R. E. (2012). A review of global terrestrial evapotranspiration: Observation, modeling, climatology, and climatic variability. *Reviews of Geophysics*, *50*(2). https://doi.org/10.1029/2011RG000373

Wang, Z., Wang, T., & Zhang, Y. (2019). Interplays between state and flux hydrological variables across vadose zones: A numerical investigation. *Water*, *11*(6). https://doi.org/10.3390/w11061295

WMO. (2019). *WMO statement on the state of the global climate in 2018*. Geneva: World Meteorological Organization.

SUPPORTING INFORMATION

Additional supporting information may be found online in the Supporting Information section at the end of the article.

How to cite this article: Rahmati M, Groh J, Graf A, Pütz T, Vanderborght J, Vereecken H. On the impact of increasing drought on the relationship between soil water content and evapotranspiration of a grassland. *Vadose Zone J*. 2020;19:e20029. https://doi.org/10.1002/vzj2.20029